Nuclear Engineering and Design 428 (2024) 113522

Contents lists available at ScienceDirect

Nuclear Engineering and Design

journal homepage: www.elsevier.com/locate/nucengdes

Neutronic and thermal–hydraulic coupling of FCM and helium annular fuel as accident-tolerant fuel

Maria Hendrina du Toit [a,*], Aubrey Mphofu [b], Ngoatladi Mashilangako [b]

[a] School for Mechanical Engineering, Faculty of Engineering, North-West University, 11 Hoffman Street, Potchefstroom 2531, South Africa
[b] Unit for Energy and Technology Systems, Faculty of Engineering, North-West University, 11 Hoffman Street, Potchefstroom 2531, South Africa

ARTICLE INFO

Keywords:
FCM
Annular fuel
ATF
Coupling
TRISO

ABSTRACT

The study aims to explore two types of Accident Tolerant Fuel (ATF) (helium annular fuel and Fully Ceramic Microencapsulated (FCM) fuel), both with Silicon Carbide (SiC) used as clad material and as a matrix material for TRISO (TRi-structural ISOtropic particle fuel) particles in FCM fuel. The safety characteristics (such as maximum fuel temperatures) were evaluated and compared against reference UO_2-Zr for a Pressurised Water Reactor (PWR) with neutronic and thermal–hydraulic coupling during normal operation for fresh fuel. The results show that both annular and FCM fuels exhibit reduced maximum temperatures compared to the reference fuel, with a reduction of 479 K (25.3 %) for helium annular fuel and 798 K (42.2 %) in the FCM fuel. The annular fuel improved the burnup by 12.4 MWd/kgU (24.2 %) without the cycle length being affected significantly (−5.6 %). The FCM fuel significantly reduced in the cycle length by 44.1 % while the burnup was more than double the reference providing a 163.5 % increased burnup in comparison to the reference fuel assembly. Assembly pin power peaking factors showed no dramatic deviation from the reference and the axial power distribution of ATFs is more symmetrical than that of the reference fuels. In terms of coupling the pin models converged after eight iterations on average with maximum relative power errors per radial node below 2 %.

1. Introduction

The Fukushima Daiichi nuclear power plant accident, initiated by the Tōhoku earthquake and tsunami on the 11th of March 2011, led to the loss of all power supply and consequential core meltdown and hydrogen explosions at three reactors (Koo et al., 2014). Today, most Light Water Reactors (LWRs) still use the same fuel pellet and zircaloy cladding combination, which provides no effective trapping mechanism for fission products once the zircaloy cladding fails. The fuel pellet's poor thermal conductivity and high power density result in a high fuel centreline temperature, making it more susceptible to melting. Zircaloy also reacts with steam, producing hydrogen that can lead to explosions similar to those in Fukushima. The core melt can also efficiently inhibit the cooling or removal of decay heat, leading to additional radioactivity barrier failures (vessel, containment/confinement) (Mizokami and Rempe, 2020).

Accident Tolerant Fuel (ATF) is a term used to describe a series of new nuclear fuel concepts, including different fuel geometries, cladding materials, and fuel pellet materials, which can improve the fuel performance of LWRs during normal operation, transient conditions, and accident scenarios. Researchers developed the ATF to enhance tolerance in accident scenarios by increasing melting points and optimising thermal conductivity for superior heat removal. ATFs use new materials that reduce or eliminate hydrogen production, enhance fission product retention, are structurally resistant to radiation and corrosion, and can withstand high temperatures during accidents (Dobisesky et al., 2014). ATF research aims to limit or circumvent fuel damage (often resulting in increased grace time before fuel degradation).

The study aims to explore two types of ATF (helium annular fuel and FCM fuel), both with SiC used as cladding material and matrix material in the case of FCM fuel for TRISO particles. For both ATF fuels, hydrogen production is eliminated due to the use of SiC cladding, which has a reduced thermal expansion, and therefore reduced pellet cladding mechanical interaction. The safety characteristics (such as maximum fuel temperatures) will be evaluated and compared against reference Pressurised Water Reactor (PWR) fuel with neutronic and thermal–hydraulic coupling during normal operation. Designing fuels that are accident tolerant should not only address the above issues but will also aim to improve burnup. Therefore, burnup will also be evaluated.

* Corresponding author.
E-mail address: marina.dutoit@nwu.ac.za (M.H. du Toit).

https://doi.org/10.1016/j.nucengdes.2024.113522
Received 23 February 2024; Received in revised form 22 July 2024; Accepted 6 August 2024
Available online 22 August 2024

1.1. Annular fuel

Massachusetts Institute of Technology (MIT) proposed annular fuel for PWRs to alleviate the problem of central heat accumulation in solid fuel pins. Their annular fuel pins provide internal and external cooling (also known as dual-cooled annular fuels) (Hejzlar and Kazimi, 2008), as shown in Fig. 1.1. The fuel diameter of annular fuel rods is significantly larger than the standard solid fuel pins to accommodate an inner channel that allows for adequate coolant flow. The increase in the diameter of annular fuel means that the number of fuel pins in an annular fuel assembly will be smaller than the conventional 17 × 17 array for solid fuel pins for a fixed fuel assembly size. Annular fuel assemblies can endure substantial power upgrades while maintaining a sufficient Departure from Nucleate Boiling Ratio safety margin (DNBR) (Ansarifar et al., 2016).

The energy generated within a solid fuel pin is transferred to the external coolant through the cladding (Feng et al., 2017). However, the energy generated in annular fuel rods is transferred to the internal and external cooling surfaces through cladding (Kianpour et al., 2020), reducing the maximum fuel temperature. Dual-cooled annular fuels with zirconium cladding bring a much higher zircaloy charge in the reactor core, which can cause a hydrogen explosion in case of severe accidents. It is vital to consider alternative fuel cladding for dual-cooled annular fuels (Deng et al., 2021).

Numerous studies of annular fuels have been published in the literature, each with different fuel pin dimensions and assembly arrays as listed in Table 1.1 (Feng et al., 2017; Silva et al., 2017; El-Sahlamy et al., 2020; Hejzlar & Kazimi, 2008; Pane et al., 2018). All these designs are based on internally and externally cooled annular fuel.

Most of the past work investigated the 13 × 13 array, which is why it was chosen for evaluating the annular fuel in this study. Table 1.2 shows the calculated hydrogen to heavy metal (H/HM) ratios for various studies as compared to the solid 17 × 17 reference. It is clear that the H/HM ratio increases with dual-cooled annular fuels.[1]

1.2. FCM fuel

Fully ceramic microencapsulated fuel consists of TRISO fuel particles embedded in a SiC matrix and has been proposed for use in the PWR as the ATF concept, as shown in Fig. 1.2. Even though TRISO fuel was designed for High-Temperature Gas-Cooled Reactors (HTGR), multiple studies have been conducted on TRISO-coated particles in LWR conditions (Deng et al., 2022; Hakim et al., 2019; Powers et al., 2013).

Deng et al. examined the neutronics and fuel cycle characteristics of FCM fuel using OpenMC, analysing flux spectra, Fuel Temperature Coefficient (FTC) and Moderator Temperature Coefficient (MTC), as well as cycle length and reactivity versus cycle length (Deng et al., 2022). Powers et al. investigated FCM fuel in LWR conditions, referencing the Westinghouse 17 × 17 fuel core, using Serpent for neutronics (including depletion analysis, flux spectra, and fuel utilisation factor) and DeCart2D/MASTER for thermal-hydraulics (Powers et al., 2013). Hakim et al. also studied the neutronic performance and fuel characteristics of FCM fuel in small modular reactors. Their analysis used Serpent and SCALE to assess FTC and MTC at the Beginning of Life (BOL) and End of Life (EOL) and compared reactivity versus cycle length (Hakim et al., 2019).

A commonality among these three references is that Uranium Nitride (UN) is usually the fuel of choice rather than uranium oxide because of its higher density' and thus more uranium atoms that can fission. All these studies tend to change the cladding material and fuel assembly arrangement to optimise parameters for sustainable negative reactivity coefficient overall (for MTC and FTC) and burnup cycle length.

The advantage of the FCM is its ability to retain fission products and increase in the time to fuel cladding failure because of the TRISO particles that are embedded in a SiC matrix, as shown in Fig. 1.2. A common shortcoming regarding the FCM fuel is that it fails to maintain its cycle length and suffers from assembly power peaking issues arising from low reactivity near the end of the cycle (Powers et al., 2013).

Multiple studies optimised fuel assembly geometry, packing methodology and fractions, enrichment, and UN kernel diameter to alleviate the problem of shorter cycle lengths (Deng et al., 2022; IAEA, 2014; Liu et al., 2016; Powers et al., 2013).

Another method to offset the decreased uranium loading in FCM fuel is to raise the packing fraction from 34 % to 74 %. Historically, a packing fraction of 60 % was achieved for the Fort St. Vrain Reactor (Brown et al., 2022). Increasing the packing fraction using conventional manufacturing methods (e.g. Chemical Vapour Deposition (CVD)) showed that the number of particles broken in their final form increases with particle packing fraction, and experimental evidence has shown that particles are more likely to touch along the axis of compression than either perpendicular to the pressing direction (Morris and Pappano, 2007).

There are two methods for increasing the packing fraction. The first is the use of multiple particle sizes. The second is the use of conventional manufacturing of TRISO particle and matrix materials using additive manufacturing (Brown et al., 2022). The latter approach was adopted for the Transformational Challenge Reactor (TCR) program sponsored by the USA Department of Energy. The approach relies on additive manufacturing to create the SiC matrix with the traditional CVD-TRISO particles (Terrani et al., 2021).

More recent studies used SiC as cladding when simulating a fuel assembly's neutronic behaviour since SiC has a small neutron capture capability, about 25 % less than Zr alloys, for the same cladding wall thickness (Liu, 2018).

1.3. SiC material properties

Understanding the material properties of the SiC is essential as it forms the matrix and the particle layers most critical to containing fission products. SiC is also used as the cladding material for both ATF fuel candidates. SiC has exceptional thermal properties, high thermal conductivity, and low thermal expansion. SiC has a smaller neutron absorption cross-section than Zirconium, due to its density being half that of Zirconium. SiC is less susceptible to degrading chemical interactions, is stable under irradiation, and does not creep below 1000 °C (Carpenter, 2006).

The SiC cladding concept has several variants: full composite cladding, a composite layer, and a monolithic ceramic layer, which can be placed on the inside or outside of the fuel rod (Singh et al., 2018). The SiC composite cladding increases maximum tolerable cladding temperatures from 2128 to 3000 K and increases corrosion resistance under normal operating conditions (IAEA, 2014). Using SiC as fuel cladding for UO_2 fuel will improve the fuel's thermal conductivity while preserving some critical UO_2 features, such as the high melting point. Adding SiC to the fuel cladding can significantly increase its thermal conductivity (Abdalla et al., 2012). Due to the higher thermal conductivity, the fuel enrichment in fuel pins with SiC cladding can be lowered, or the enrichment can be kept unchanged. At the same time burnup is increased, which can significantly benefit fuel economy (Slabber, 2014).

In the FCM fuel, the most critical material of significant concern is the SiC matrix and layer because there are many fabrication routes. These different fabrication routes result in different mechanical properties. Various fabrication methods exist, such as sintering, direct conversion, gas phase reaction and polymer pyrolysis for synthesising SiC. The chemical vapour CVD techniques are primarily used to manufacture the SiC layer and produce highly crystalline, stoichiometric and high-purity β-SiC (Snead et al., 2007).

Another standard fabrication route is a liquid phase sintering method called the Nano-Infiltration Transient Eutectic (NITE) phase process.

[1] Guide tube dimensions for all arrays were kept constant.

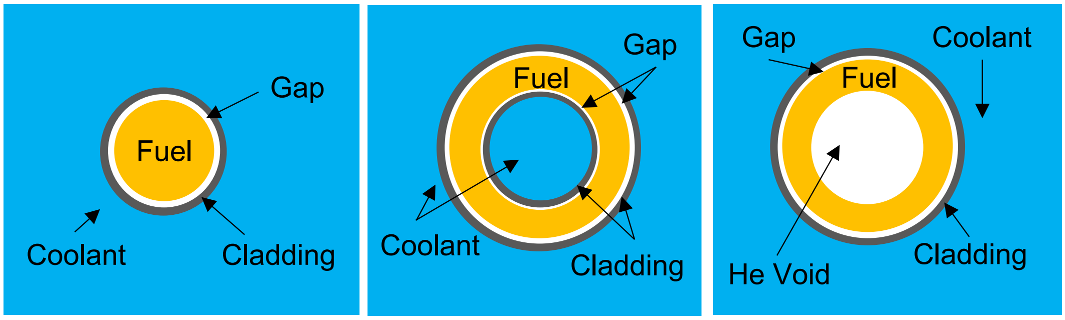

Fig. 1.1. a) Solid pin, b) dual-cooled annular pin, and c) helium annular pin.

Table 1.1
Various studies on annular fuels.

Reference	Fuel assembly array	
	Solid fuel	Annular fuel
(Feng et al., 2017)	17 × 17	15 × 15
		14 × 14
		13 × 13
		12 × 12
		11 × 11
(Silva et al., 2017)	16 × 16	15 × 15
		14 × 14
		13 × 13
(Hejzlar and Kazimi, 2007)	17 × 17	13 × 13
		12 × 12
(El-Sahlamy et al., 2020)	17 × 17	13 × 13
(Deng et al., 2021)	–	13 × 13
(Ellis, 2006)	17 × 17	13 × 13
(Pane et al., 2018)	17 × 17	13 × 13

Table 1.2
H/HM for pin and fuel assembly for 13x13 dual-cooled annular fuels.

	H/HM pin	H/HM FA
(Zhuchkovaa and Nava-dominguez, 2014)	7.673	8.237
(Silva et al., 2017)	8.192	8.746
(Hejzlar and Kazimi, 2007)	7.673	8.205
(Ellis, 2006)	7.673	8.205
(El-Sahlamy et al., 2020)	7.672	8.204
Solid 17 × 17	4.887	5.598

The dual-cooled fuel has two surfaces that need cladding and has implications for manufacturing, cost, neutron absorption, and flow distribution. Since the cladding surface of water annular fuel is increased significantly and the end welds are more complicated, this could potentially increase the fuel pin leak statistics (Yueh and Terrani, 2014). Therefore, it was decided to replace the water and the inner cladding with a helium void. Replacing the water will also assist in decreasing the H/HM, which will resemble a value closer to the solid 17 × 17 reference. Yarmohammadi et al. also used an annular fuel pin to study the effect of the annular hole on the fuel temperature distribution. The maximum fuel temperature of the annular fuel was 150 K less than that of the reference fuel pin (Yarmohammadi et al., 2017). It must be noted that helium annular fuel will require each fuel pellet to be sealed at the top and bottom to maintain the helium pressure inside the annulus.

This method produces a dense SiC matrix, which is hot-pressed and processed to obtain the FCM pellets. The method uses fewer oxide additives and allows for lower temperature treatment (200–400 °C), which achieves properties close to the CVD SiC. Manufacturing methods dramatically affect the thermal and mechanical properties of SiC under non-irradiated and irradiated conditions (Deng et al., 2022). The NITE fabrication method is used only for the SiC matrix, while the SiC particle layer is fabricated with the CVD method. They both have similar material qualities and are assumed to have the same diffusion of fission product rates. This assumption will be used to carry out the simulation and is assumed because of the lack of consensus on NITE-SiC matrix material properties (Schappel, 2017).

Fig. 1.3 shows the thermal conductivity of different fabricated SiC as a function of temperature. The importance of Fig. 1.3 comes from the grain size of the SiC, as Snead et al. note that thermal conductivity also depends on the nature of the grain boundaries. For example, a hot-pressed SiC has poorer thermal conductivity. This can be attributed to the sintering additives (considered impurities in the SiC form) that have lower thermal conductivities than the SiC material (Snead et al., 2007).

2. Methodology

This section outlines the simulation methodology and parameters for the three fuels: the reference fuel based on the North Anna geometry, the helium annular fuel with SiC cladding, and the FCM fuel with SiC matrix and cladding. The North Anna reference model was verified and validated before comparing the proposed ATFs. The study compared the two proposed ATF candidates' maximum temperature and cycle length against the reference fuel. To compare the cycle length, fuel assembly burnup calculations were carried out (Section 2.2). Coupled calculations on a pin level are carried out for an average fuel pin channel at BOL (fresh fuel) (Section 2.3) to determine the maximum fuel temperature.

The assessment of the different fuels relies on maintaining the same power level, fissile content, coolant flow rate and dimensions across all three fuel assembly models, allowing for minimal core modifications. However, this means varying power densities in fuel pins due to differences in enrichment, fuel mass, and number of pins per assembly. The enrichments were calculated and listed in Table 2.1 based on keeping the ${}^{235}_{92}U$ loading constant.

2.1. Codes

The neutronics code used for this study was Serpent for eigenvalue and burnup calculations. Serpent is a Monte Carlo three-dimensional continuous-energy reactor physics burnup code under development at VTT Technical Research Centre in Finland. Serpent calculates burnup using self-contained built-in depletion solvers. To speed up the calculation for each burnable material after the simulation is completed, the continuous-energy cross-section with flux spectra is collapsed, and this method is known as spectrum-collapse (Leppänen et al., 2014). Serpent can also perform coupled multi-physics applications (Kaltiaisenaho, 2020).

The thermal-hydraulics code used for this study was Flownex. Flownex is a steady state and dynamic systems simulation code based on Computational Fluid Dynamics (CFD) solving techniques. It uses a fully implicit pressure–velocity coupling to solve the momentum equation in each element and the energy and continuity equation at each node. In the nuclear industry, Flownex estimates heat transfer, mass flows, and pressure in the reactor core during normal operating and accident conditions (van Ravenswaay et al., 2006). Due to Flownex's ability to model coolant density and temperature, as well as fuel temperatures, it

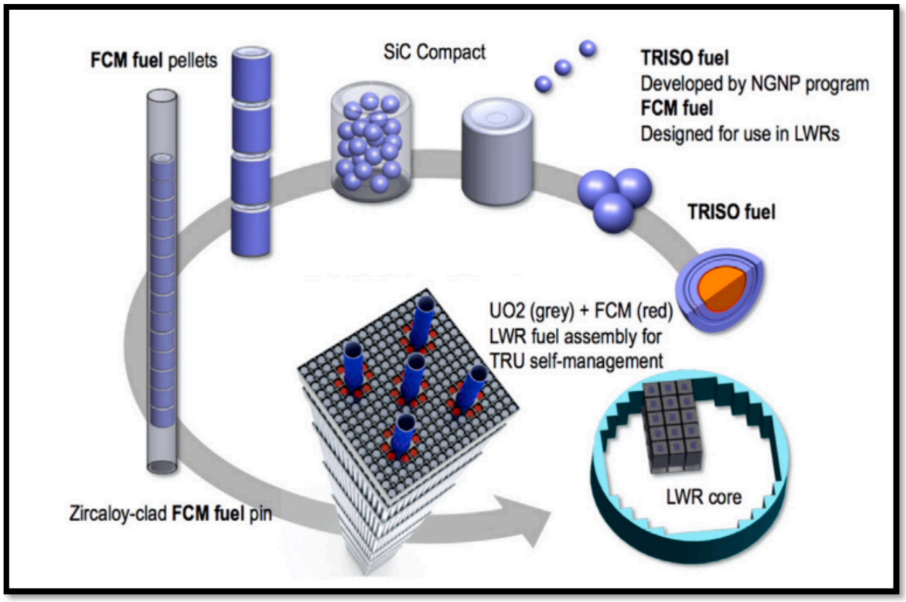

Fig. 1.2. FCM fuel in LWR (Powers et al., 2013).

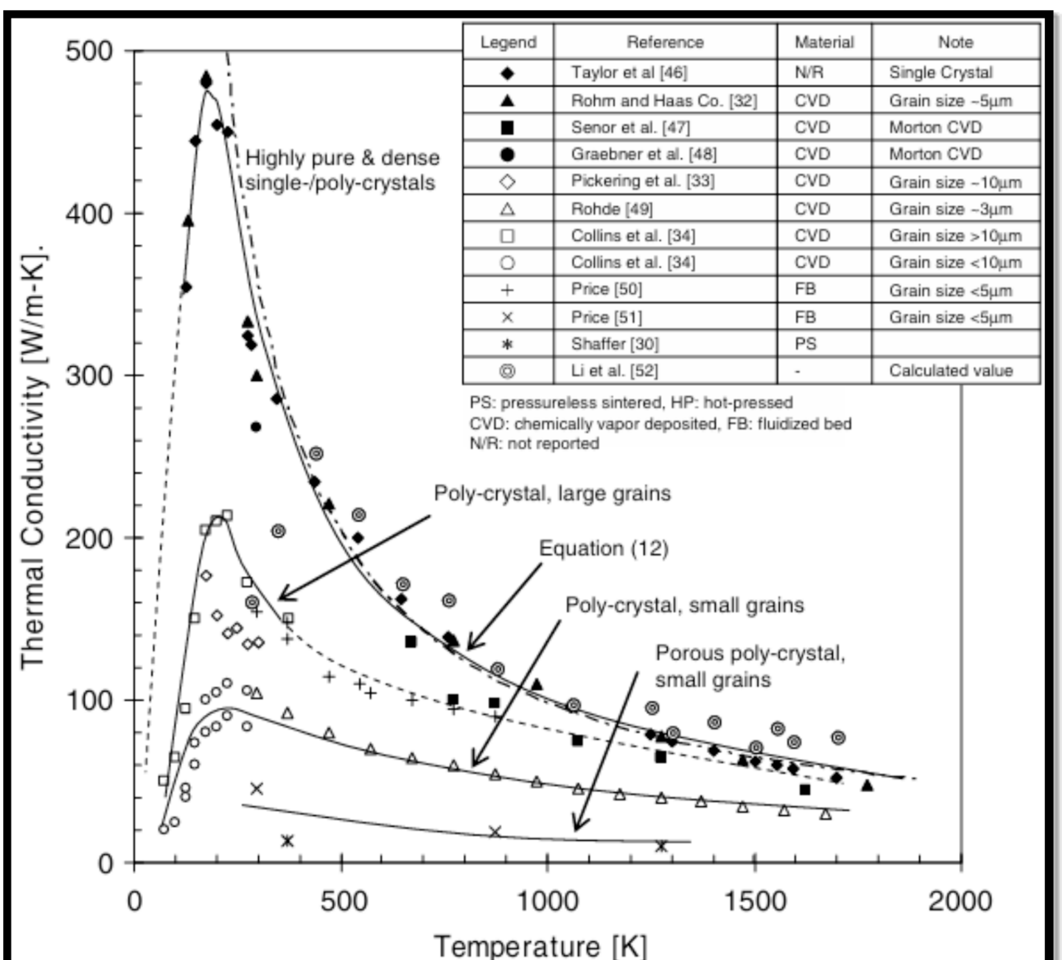

Fig. 1.3. Thermal conductivity of SiC at elevated temperatures (Snead et al., 2007).

Table 2.1
Enrichment for reference, helium annular and FCM fuel.

Fuel	Reference fuel	Helium Annular	FCM
Enrichment	3.1 wt%	4.043 wt%	14.668 wt%

was utilised in this study for the thermal–hydraulic calculation. The Distributed Heat Source (DHS) element in Flownex simulates heat generation within a volume/material (Flownex 2022).

Both Serpent (Ćalić et al., 2016) and Flownex (Van Der Merwe et al., 2006) have been validated and widely used for nuclear applications.

2.2. Burnup

A medium-enriched (3.1 wt%) fuel assembly of the reference reactor was chosen as representative of the full core. The three fuel types were modelled on a fuel assembly level for burnup calculations. Fig. 2.1 shows the reference fuel assembly with fuel pins and the guide tubes filled with water.

The reference fuel assembly was burned for three cycle lengths as defined in the Safety Analysis Report (SAR) to determine the End of Cycle (EOC) criticality. All the burnup models use the same constant temperatures as specified in Table 2.6. Continuous nuclear data were utilised from the ENDF/B-VII.1 library. All three fuel assembly models' burnable fuel material was divided into eight radial depletion sub-zones. The fuel assemblies were modelled in 3D, with boundary conditions for the 17 × 17 and 13 × 13 fuel pin arrays reflective in the x and y directions and black (vacuum) in the z-direction. Table 2.2 lists the neutronic settings used for the neutronic Monte Carlo calculation.

2.2.1. Reference

The North Anna PWR reactor is well documented and was selected as the reference (Mulasi, 2022). The core contains 157 Fuel Assemblies (FA), and each fuel assembly is arranged in a 17 × 17 lattice. Each fuel assembly consists of 264 fuel rods and 24 guide tubes, and grids support these fuel rods at intervals along their length to maintain spacing between the rods in the assembly. Control rods are withdrawn and a boron concentration of 0 ppm. Since the power output of the full core North Anna reactor is 2893 MWth and the reactor has 157 fuel assemblies, the power is divided by the number of assemblies to get the power per assembly (which is constant for all models). The fuel rods are cladded by Zircaloy-4, and the main reactor properties are listed in Table 2.3.

Table 2.2
Monte Carlo parameters used in serpent for fuel assemblies.

Design Parameters	Reference	Annular	FCM
Number of source points	100,000	100,000	100,000
Number of active cycles	2500	2500	2500
Number of inactive cycles	400	400	400
Statistical error	9.2 pcm	4 pcm	9.8 pcm

Table 2.3
North Anna Reactor Design Configuration (NRC, 2016).

Design Parameters	Numbers/Material	Units	Reference
Thermal power	2898	MWth	(NRC, 2016)
Coolant temperature inlet	559.15	K	
Peak temperature centreline	2060.92	K	
Pressure drop core	163.40	kPa	
Nominal pressure	15.513	MPa	
Active fuel height	364.998	cm	
Assembly pitch	21.50364	cm	
Pin pitch	1.25984	cm	
Cladding radius	0.409575	cm	
Cladding thickness	0.057	cm	
Pellet radius	0.4095	cm	
Guide tube inner diameter	1.143	cm	
Guide tube outer diameter	1.22428	cm	
Cladding material	Zircaloy-4	–	
Gap gas	Helium	–	
Theoretical Density (TD)	95	%	(Feng et al., 2017)
Fuel density	10.412	g/cm^3	

2.2.2. Helium annular

The suggested dimensions from previous studies (Table 1.1) for a 13 × 13 array were modified for the helium annular fuel by replacing the internal coolant channel with a helium void. The H/HM for various geometries ranged from 3.83 to 5.48, which resembles the reference (5.60) more closely than compared to the dual-cooled annular fuels. Note that for helium annular fuels, the H/HM immediately reduces due to the removal of the inner water channel. The inner and outside radii were then varied to closely match the H/HM ratio of the North Anna fuel reference.

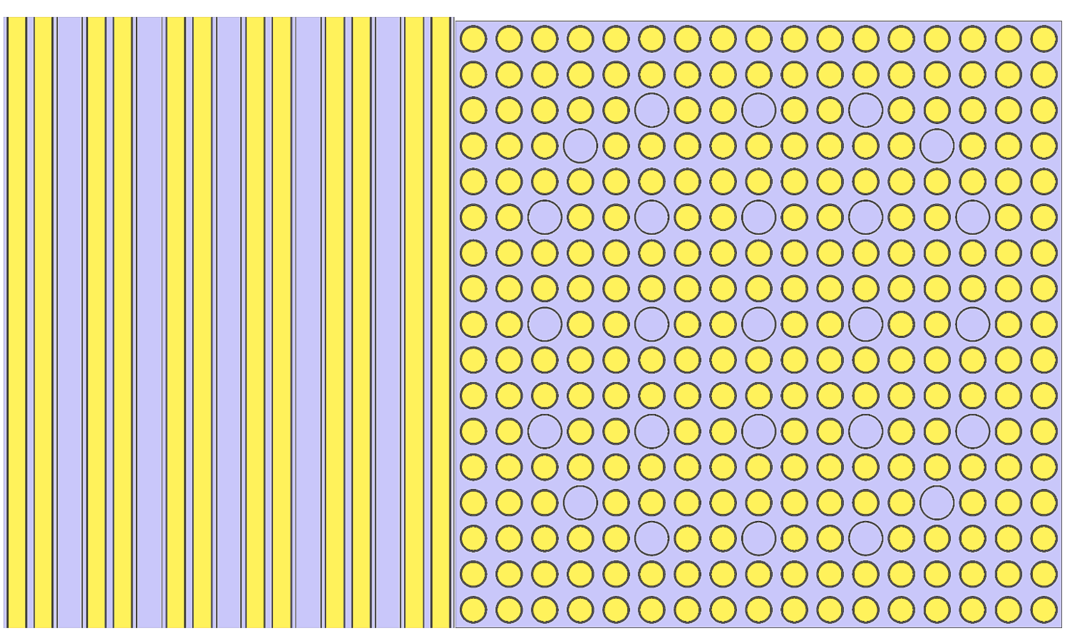

Fig. 2.1. Side view and top view of the reference 17 × 17 fuel assembly.

Table 2.4
Helium annulus pin and assembly dimensions.

Parameters	Numbers	Units	Reference
Array	13x13	–	–
Dfi	1	cm	
Dfo	1.36	cm	
Dci	1.3848	cm	
Dco	1.4991	cm	
Pin pitch	1.646	cm	
H/HM pin	4.3489	–	
R in guide	0.7	cm	
R out guide	0.7684	cm	
Fuel assembly pitch	21.398	cm	
H/HM Assembly	4.9709	–	
Gap gas	Helium	–	
Cladding material	Silicon carbide	–	
Theoretical Density	94	%	(Feng et al., 2017)
Fuel density	10.302	g/cm^3	

Table 2.4 contains the adapted helium annulus fuel pin, assembly dimensions, and the H/HM ratio. The H/HM per assembly is 4.35, which is lower than the reference of 5.60. The guide thimble and tube dimensions for this model were adapted from literature. The subscripts ci, f, and co designate inner cladding, fuel, and outer cladding; the second subscript designates the outer (o) or inner (i) surface.

Fig. 2.2 presents the top and side views for the fuel pin. The yellow circle represents the fuel pellet, the helium gaps are white, the coolant is blue, and the SiC cladding is dark grey.

2.2.3. FCM

The material compositions of the various materials were taken from the Serpent built-in material libraries. The dimensions used for the TRISO particle are from the Micro Modular Reactor (MMR) by the USNC (Keun et al., 2014), as shown in Table 2.5. It is important to note that the buffer, IPyC (Inner Pyrolytic Carbon) and OPyC (Outer Pyrolytic Carbon) layers are materially composed of carbon only, and their density is the only difference between them. A packing fraction of 58 % was used, and SiC was used as the cladding.

Fig. 2.3 illustrates the FCM fuel pin, which uses the following colours for different materials: UO_2 fuel is yellow, the SiC matrix and layers are dark grey, IPyC and OPyC are red, the buffer layer is light blue, the water outside of the pin is purple, the helium is white and next to the water is the lighter grey SiC cladding.

Table 2.5
TRISO particle material properties used for simulation.

Parameters	Numbers	Units	Reference
Kernel radius	0.04	cm	(Keun et al., 2014)
Buffer layer thickness	0.007	cm	
IPyC layer thickness	0.0035	cm	
SiC layer thickness	0.0035	cm	
OPyC layer thickness	0.0020	cm	
Buffer layer density	1.0	g/cm^3	
IPyC & OPyC layer density	1.9	g/cm^3	
SiC layer & matrix density	3.2	g/cm^3	
UO_2 density	10.412	g/cm^3	(Feng et al., 2017).
Theoretical density	95	%	
TRISO packing fraction	58 %	–	Maximum feasible packing in Serpent
Gap gas	Helium	–	(NRC, 2016)
Cladding material	SiC	–	–

2.2.4. Results

Fig. 2.4 depicts the k_∞ values with burnup. Here, it is evident that the FCM fuel starts with a notably higher k_∞ at 1.62961, which was 29,570 pcm higher than the reference case. This elevated value can be attributed to its high enrichment level when compared with both the annular and the reference fuels. The higher k_∞ of FCM fuel necessitates the increase in boron concentration and burnable absorbers in the fuel, which might negatively affect the neutron economy compared to fuels that do not require so much reactivity management.

As the cycles progress to the EOC, the data revealed that the FCM fuel continued to exhibit superior performance, achieving a higher burnup at 130.73 MWd/kgU compared to the reference and annular fuels at 51.25 and 63.64 MWd/kgU respectively. The burnup for FCM was more than twice as large as for the reference case. The higher burnup can be attributed to the reduction in UO_2 for the FCM fuel, which makes up only 52 wt% of the FCM fuel. The annular fuel achieved a cycle burnup improvement of 12.4 MWd/kgU (24 %) compared to the reference.

Fig. 2.5 shows the reactivity change with time for three cycles. The trend is similar to Fig. 2.4 in that the k_∞ at BOL for FCM fuel is higher than the other fuels, but it can be seen that the length of three cycles for the FCM fuel is much shorter than for the annular and reference fuel.

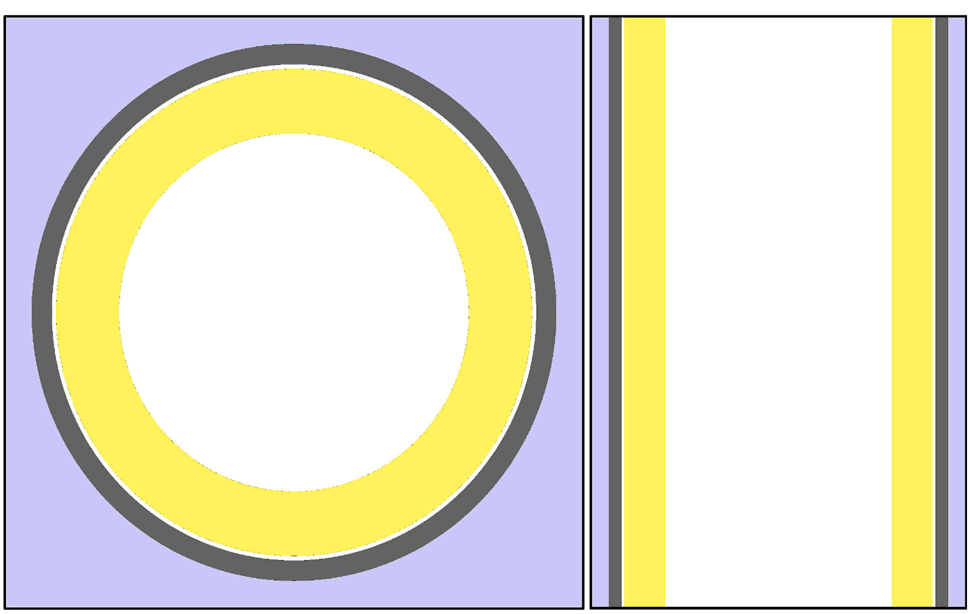

Fig. 2.2. Helium annulus pin (a) top view, (b) side view.

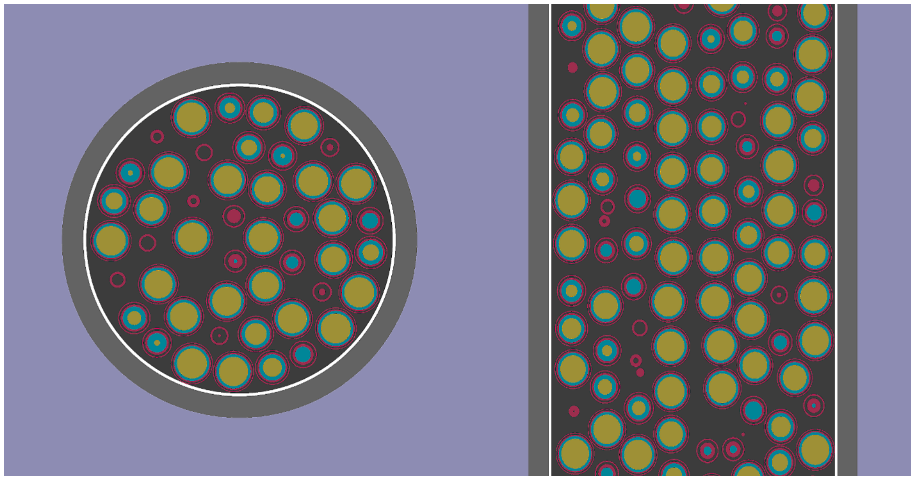

Fig. 2.3. FCM pin (a) top view, (b) side view.

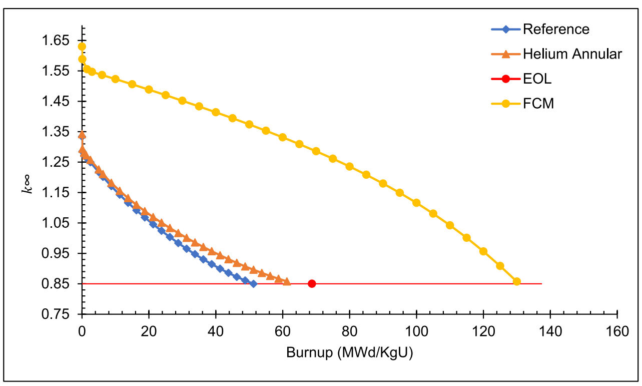

Fig. 2.4. Variation of k_∞ with burnup for fuel assemblies.

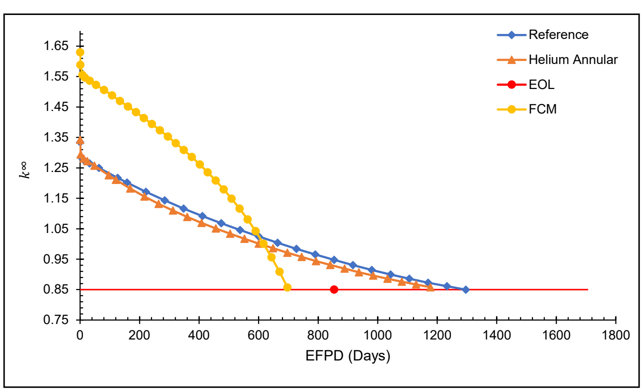

Fig. 2.5. Variation of k_∞ with EFPD for fuel assemblies.

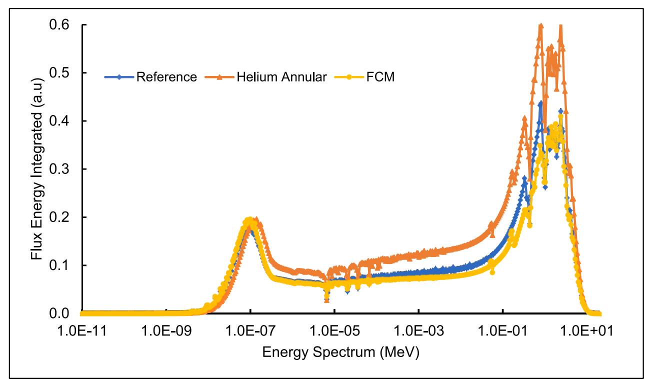

Fig. 2.6. Neutron flux spectrum at BOL for fuel assemblies.

Three cycles for FCM resulted in 701 effective full power days (EFPD) as compared to 1296 EFPD for the reference, which means that a three-batch cycle for FCM fuels is less than half of that of the reference. Reduced cycle length affects the economics negatively. Nonetheless, if UN is replaced with UO_2 the cycle length could be extended since UN is denser (13.5 vs 9.6 g/cm^3) (Bright and Eleanor, 2019). The fuel cycle length for the annular and reference was quite similar to the reference (1223 EPFD), with a slightly reduced life of 73 days (or −5.6 % reduction) over three cycles. These fuels exhibit different cycle lengths with the same ^{235}U loading due to the resultant spectrums and breeding within ^{238}U. FCM fuel has a reduced ^{238}U loading due to the increase in enrichment, which will reduce the breeding potential of ^{239}Pu.

Fig. 2.6 shows the neutron flux spectrum at the BOL of the three fuels. It is seen that the FCM fuel had the most thermalised neutrons available at the BOL, followed by the reference fuel and then the helium annular fuel. The helium annular fuel had the hardest spectrum of all three fuels. The H/HM for helium annular fuel was slightly lower than for the reference fuel, due to the replacement of helium in the central hole where fuel is supposed to be, a lower H/HM ratio resulted in a slightly harder spectrum. A harder spectrum promotes the breeding of ^{239}Pu, and resultantly, the annular fuel achieved a slightly higher burnup. The H/HM ratio for the FCM fuel was much higher than for the other two fuels due to a lower amount of heavy metal in the fuel (because of the higher enrichment) with the same water content, which made the spectrum softer (together with some graphite moderation in PyC layers). The softer spectrum and the lower amount of ^{238}U resulted in weaker conversion/breeding in the FCM fuel and therefore shorter cycle length.

Fig. 2.7 shows the power distribution in a fuel assembly for fresh fuel for the reference. It can be seen that the relative peak power per pin for the reference was 1.07. The power factors next to the control rods are slightly elevated due to enhanced moderation in the water-filled guide tubes which enhances the fission power.

The relative peak power per pin was 1.072 for FCM fuel (See Fig. 2.8), which was slightly higher than the reference (1.07). It is important to note that the average pin power of the FCM and reference fuel was the same due to a similar 17 × 17 lattice. The annular fuel assembly in Fig. 2.9 had a relative pin peak power of 1.085 (compared to the average pin power), which was 1.4 % higher than the reference and insignificant. The average power per helium annular pin was about 1.65

0.9	0.907	0.917	0.93	0.944	0.957	0.955	0.953	0.959	0.952	0.953	0.955	0.943	0.931	0.916	0.908	0.902
0.906	0.914	0.932	0.957	0.977	1.013	0.986	0.984	1.016	0.985	0.986	1.015	0.978	0.954	0.93	0.913	0.907
0.916	0.931	0.968	1.024	1.047		1.039	1.037		1.037	1.041		1.047	1.025	0.969	0.932	0.917
0.931	0.955	1.026		1.069	1.062	1.018	1.016	1.047	1.015	1.018	1.065	1.068		1.025	0.954	0.931
0.944	0.978	1.048	1.069	1.047	1.066	1.022	1.023	1.055	1.022	1.022	1.063	1.048	1.071	1.048	0.979	0.944
0.954	1.013		1.061	1.065		1.059	1.056		1.056	1.059		1.065	1.064		1.014	0.955
0.954	0.984	1.04	1.018	1.023	1.058	1.023	1.024	1.058	1.025	1.023	1.059	1.022	1.019	1.04	0.985	0.953
0.953	0.984	1.035	1.016	1.02	1.057	1.023	1.024	1.058	1.023	1.024	1.056	1.02	1.013	1.038	0.986	0.954
0.959	1.015		1.048	1.053		1.056	1.058		1.059	1.055		1.054	1.049		1.016	0.958
0.954	0.984	1.036	1.015	1.019	1.055	1.022	1.023	1.057	1.024	1.024	1.059	1.02	1.013	1.037	0.987	0.952
0.952	0.983	1.039	1.019	1.024	1.056	1.021	1.023	1.056	1.021	1.025	1.057	1.022	1.017	1.04	0.986	0.954
0.955	1.014		1.063	1.065		1.058	1.056		1.055	1.058		1.065	1.061		1.016	0.957
0.944	0.978	1.048	1.07	1.049	1.064	1.023	1.02	1.053	1.02	1.024	1.064	1.047	1.068	1.048	0.978	0.943
0.93	0.954	1.022		1.07	1.061	1.019	1.012	1.046	1.015	1.018	1.064	1.068		1.024	0.952	0.931
0.918	0.932	0.967	1.021	1.047		1.038	1.037		1.037	1.039		1.049	1.023	0.967	0.931	0.916
0.905	0.916	0.93	0.955	0.978	1.013	0.985	0.984	1.014	0.985	0.985	1.013	0.979	0.954	0.933	0.915	0.907
0.9	0.906	0.917	0.93	0.944	0.955	0.953	0.953	0.96	0.953	0.953	0.955	0.943	0.93	0.917	0.905	0.9

Fig. 2.7. Reference assembly pin power factors.

times larger than the FCM and reference fuel due to a reduced 13 × 13 lattice. Therefore, it can be inferred that the expected peak power for the annular fuel should be higher. Fortunately, the pin peak power was not much higher due to the effect of the annular hole and reduced water in the equivalent pin channel. The power distribution and peaking are dependent on the resolution of the grid, for instance, a finer grid can lead to a more evenly distributed power across the fuel assembly. Nonetheless, the pin power peaking factors are not significant for the proposed ATFs.

2.3. *Coupling*

2.3.1. *Methodology*

Coupling is the process of combining neutronic and thermal–hydraulic physics. The coolant's thermal–hydraulic parameters substantially influence nuclear reactors' neutron spectrum, cross-sections, flux and power distribution. The neutronic code determines the neutron spectrum and power, and the thermal–hydraulic code estimates the coolant parameters such as density and temperature (Safavi et al., 2020).

Coupling can be achieved internally or externally. Two codes are integrated into the internal coupling, and the data transfer occurs within the integrated code. The internal coupling method provides a high level of accuracy and parallelism. The disadvantage of this method is that enormous code modification is required, and there is limited access to source codes. External coupling is accomplished through a user interface module, transferring data between two codes without modification. The advantage of the external method is that both codes can maintain their independence during the procedure (Ye et al., 2020). The drawbacks of external coupling are slower convergence and human error. Due to its simplicity, the external coupling method was applied in the study. The coupling procedure is shown in Fig. 2.10 and described in the steps below:

1. The process was initiated with a 3D pin Serpent criticality calculation.
2. The temperature and density distribution of the coolant in the first iteration were assumed constant at ten axial nodes, as seen in Table 2.6. The cool.ifc file was created and linked to the respective fuel pin input file. The same axial discretisation (10) was applied in all three fuels.
3. The fuel.ifc file was created and linked to the respective fuel pin input file. The temperature of the eight radial rings in the fuel pin was specified in this file. See Table 2.6 for the specification of the constant fuel temperature for the first iteration.
4. The Serpent input was run, which produced the detector file with the power distribution at each axial node.
5. The Flownex model was set up, and all parameters and material compositions were specified as described in Section 2.3.2-2.3.3.
6. The axial power distribution from the detector output was used in the Flownex input file to specify the axial power distribution for the thermal-hydraulics calculation.
7. Steady-state conditions were run with Flownex, which produced two output files. The first file contains axial coolant densities and temperatures. The second file represents the fuel temperatures in ten axial and eight radial nodes, as well as gap and cladding temperatures.

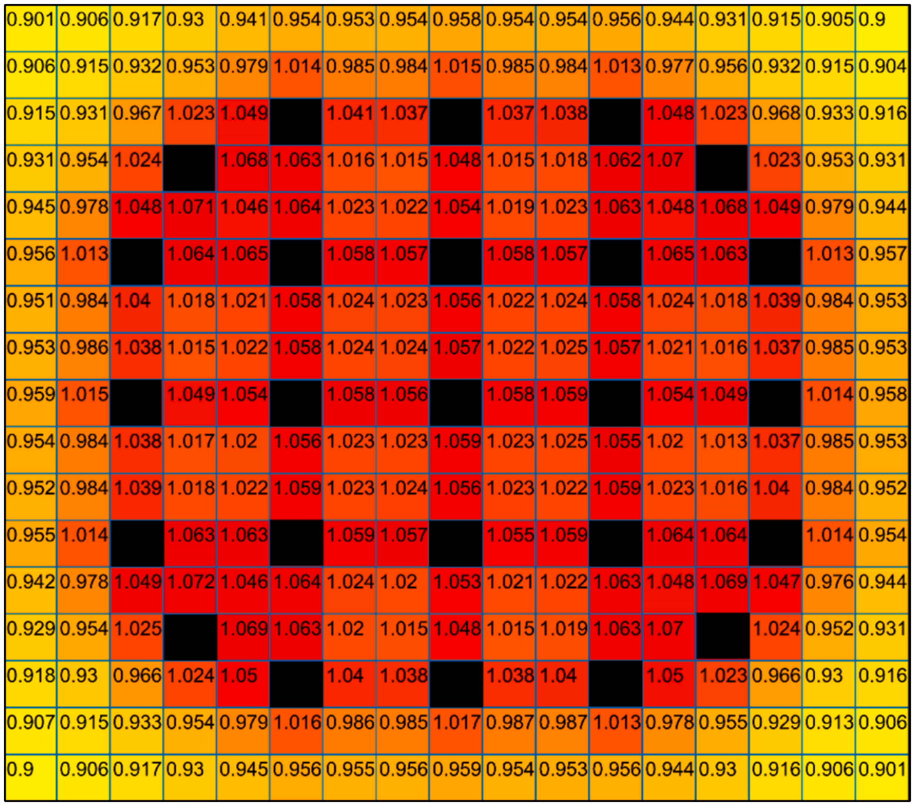

Fig. 2.8. FCM assembly pin power factors.

Fig. 2.9. Helium annular assembly pin power factors.

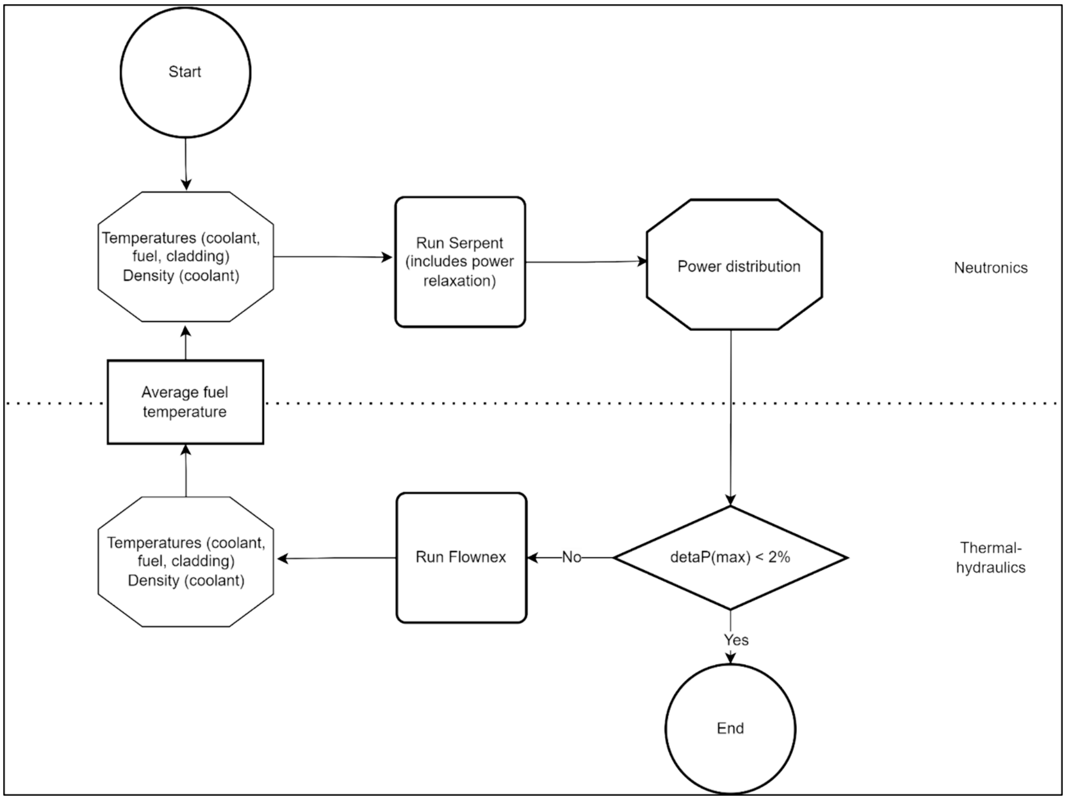

Fig. 2.10. Coupling methodology between Serpent and Flownex.

Table 2.6
Average temperatures of different materials (Bowman and Suto, 1996).

Material	Temperature (K)
Fuel	901
Cladding	629
Water	583

8. The new fuel temperatures produced by Flownex were averaged between the current and previous iteration results to prevent the solution from diverging. The averaged axial and radial fuel distribution was transferred to the fuel.ifc file.
9. 9 The coolant densities and temperatures from Flownex were input into Serpent cool.ifc file.
10. Serpent calculated a new power distribution at the updated temperatures. Serpent utilises a stochastic approximation technique to improve power convergence. At each iteration n, the power distribution was determined as:

$$P^n_{rel} = P^{n-1}_{rel} - \frac{s_n}{\sum_i^n s_n} d(P^{n-1}_{rel} - P^n) \tag{2.1}$$

Here P^n is the initial power distribution of iteration n,while P^{n-1}_{rel} represents the adjusted power distribution from the prior iteration. S_i signifies the active neutron population at iteration i, and d stands for the under relaxation factor, modifiable via the 'set relfactor' option. For all simulations, a relaxation factor of 0.5 was used for Equation (2.1) (Valtavirta, 2017).

11. Steps 1–10 were repeated, and the iteration process continued until convergence was reached. Convergence was achieved when maximum power errors (per axial node) were ≤ 2 % relative to the previous iteration.

Note that the gap and cladding temperatures were not transferred between the thermal–hydraulic and neutronic codes since the gap and cladding materials do not affect the neutronics/power solution significantly. The degradation of fuel pellet thermal conductivity is not accounted for since the coupling is only carried out at BOL.

2.3.2. *Neutronic model*

The neutronic pin model is similar to the fuel assembly with dimensions found in Table 2.3. A fuel pin is modelled in 3D for fresh fuel, with boundary conditions reflective in the x and y directions and black in the z-direction. The number of source points, the number of skipped and active are listed in Table 2.7, which resulted in statistical errors not larger than 15 pcm. Source convergence was confirmed by inspecting the plots for the Shannon entropy.

2.3.3. *Thermal-hydraulic model*

The temperatures of all the materials used at the start of coupling are listed in Table 2.6. The temperatures were assumed constant in radial and axial directions for the first calculation but changed with each consecutive coupling iteration. A single fuel channel was set up using the Flownex Pipe element to simulate the coolant flow and coupled with the DHS to represent the fuel, gap, and cladding. Grid independence was

Table 2.7
Parameters used in Serpent and Flownex for reference, FCM and annular pins.

Design Parameters	Reference	FCM	Helium annular	Units
Number of source points	100,000	100,000	40,000	–
Number of active cycles	2500	2500	800	–
Number of inactive cycles	400	400	450	–
Statistical error	9.2	9.8	15	pcm
Power Relaxation factor	0.5	0.5	0.5	–
Wetted perimeter	3.369	3.369	4.95	cm
Mass flow	0.2796	0.2796	0.4782	kg/s
Power per pin	69.79	69.79	115.17	kW

obtained in the fuel pin using 25 radial nodes. An adiabatic boundary condition at the central radius position was assumed for all three fuels.

UO_2

The Flownex input requires thermal conductivity for the fuel (UO_2). Equation (2.2) was used to compute the thermal conductivity at different temperatures (Kavazauri et al., 2016).

$$\lambda\left[\frac{W}{m.K}\right] = \frac{100}{7.5409 + 17.692\tau + 3.6142\tau^2} + \frac{6400}{\tau^{5/2}}\exp\left(\frac{-16.35}{\tau}\right) \tag{2.2}$$

where $\tau = T/1000$ and T is the temperature (K).

Equation (2.3) is recommended for the correlation of UO_2 heat capacity. Table 2.8 provides the values of the constants used in Equation (2.3) (Popov et al., 2000).

$$C_P(T)\left[\frac{J}{Kg.K}\right] = C_1\left(\frac{\theta}{T}\right)^2 \frac{\exp\left(\frac{\theta}{T}\right)}{\left[\exp\left(\frac{\theta}{T}\right) - 1\right]^2} + 2C_2T + C_3E_a\exp\left(-\frac{E_a}{T}\right)/T^2 \tag{2.3}$$

where T is the temperature (K), θ is Einstein temperature (K) and E_a is the electron activation energy divided by the Boltzmann constant (K).

Gap

Zircaloy-4 cladding is sealed with helium gas in the gaps under pressure equal to or more than 2.5 MPa (Gabr et al., 2003). The gap thermal conductivity and heat capacity were computed at 2.5 MPa. Flownex has thermal conductivity and heat capacity for helium built-in at 2 and 3 MPa. The average thermal conductivity and heat capacity of helium at 2 MPa and 3 MPa were used.

Zircalloy-4

Flownex has a Zirconium built-in material library. Zircaloy-4 is one of the Zirconium alloys, and the properties are assumed to be the same.

SiC cladding

As shown in Fig. 1.3, the thermal conductivity of SiC varies a lot based on the manufacturing method. To be conservative, data was extracted from Fig. 1.3, representing one of the lower curves with polycrystal small grains for thermal conductivity.

Water

Flownex uses two-phase H_2O from the master database. The flow through the guide tubes was accounted for when calculating the coolant flow rate in each fuel channel. The fuel assembly flow rate was divided by 289 channels to get the flow through one channel. Similarly, the flow area of the whole fuel assembly was calculated (including the flow area of the guide tubes), which was then normalised to one channel by dividing it by the number of channels.

FCM

The density and thermal conductivity properties of TRISO layers were sourced from Keun et al. (Keun et al., 2014). The thermal–hydraulic model treated the FCM fuel as homogeneous, using mass weighting of all the individual materials to calculate its heat capacity, thermal conductivity of the homogeneous mixture. The density of the homogeneous mixture was also calculated in the same manner from individual densities in Table 2.5.

The Serpent interface files do not support radial or axial temperatures through a point-average interface, as the material specifications in Serpent require homogeneity. Consequently, the fuel temperature was uniformly averaged along the axial sections, and a singular temperature was applied across the radial dimension for each axial node, conforming to Serpent's regular mesh-based interface (Leppänen, 2011).

It was not feasible to pinpoint individual temperatures for separate FCM layers of each TRISO particle using the current codes of SERPENT and Flownex. CFD software is required for a more accurate temperature distribution (Scolaro et al., 2022). However, this is suggested for future studies.

Table 2.9 shows the specific heat capacity, thermal conductivity and mass weighting used for the different layers of the FCM fuel in order to determine the homogeneous FCM fuel properties for Flownex.

Fig. 2.11 was plotted to examine the thermal conductivity of the FCM and reference fuel of North Anna based on the Table 2.9. From Fig. 2.11 it can be seen that the thermal conductivity of FCM is superior to the reference fuel which affects the radial and axial temperature distribution thus it should be inferred that the temperature distribution will be a smoother gradient than reference fuel resulting in lower peak temperatures.

Table 2.8
Constant used in heat capacity (Popov et al., 2000).

Constant	UO_2	Units
C_1	302.27	J/Kg/K
C_2	8.463×10^{-3}	J/Kg/K^2
C_3	8.741×10^{7}	J/Kg
θ	548.68	K
E_a	18531.7	K

2.3.4. Results

This section presents the maximum power errors for every iteration to evaluate the behaviour of power convergence. The power distribution along the axial direction is presented with the temperature distribution in the radial and axial directions.

Fig. 2.12 shows that the reference fuel pin, helium annular, and FCM fuel converged after 13, 5 and 6 iterations, respectively. The reference fuel, helium annular, and FCM fuel achieved maximum power errors of 1.67 %, 0.7 % and 2 %, respectively. The reference fuel reached a maximum power error of 3.05 % after iteration 4, however the axial power profile was not representative, and therefore a more stringent convergence criterion (<2%) was chosen. The FCM fuel converged earlier than the reference fuel since the homogeneous temperature for each axial node was coupled. In contrast the other two fuels were coupled radially and axially.

Fig. 2.13 illustrates the power distribution along the axial direction of the respective fuels where Node 1 is the water inlet (at the bottom), and Node 10 is at the outlet at the top. The annular fuel exhibited a unique power distribution due to its inherent design features. This fuel variant produced more power per rod than the FCM and reference fuels, which is attributed to its 13 × 13 fuel assembly lattice. The maximum power for both ATFs was located at axial Node 4 where the reference fuel peaked higher at Node 3. The power peaks more towards the lower part of the core due to lower temperature and higher densities of the coolant. Assuming a uniform fissile material distribution at BOL, enhanced moderation at the bottom will result in higher fission power.

The axial power distribution profiles of the two ATF types are more symmetric than that of the reference LWR fuel. A possible explanation would be the fact that both the FCM and SiC cladded annular fuel have enhanced thermal conductivity due to the higher thermal conductivity of SiC. Note that these profiles will shift as the burnup progresses. The maximum power per axial node for the FCM fuel was 10571 W which was quite similar (0.5 % difference) to the reference fuel at 10620 W. The helium annular fuel has a maximum power per axial node of 17890 W, which is 1.685 times higher than the reference. This increase was expected since the power per pin for annular fuel is 1.65 times larger than the reference due to the 13 × 13 lattice (the number of pins per assembly is reduced).

Fig. 2.14 shows the axial fuel temperature, and it can be seen that the reference fuel had the highest fuel temperature which was located at axial Node 4. The maximum temperature was located in the fourth and fifth node, respectively for the annular and FCM fuel. The annular fuel and the FCM fuel behaved similarly with significantly reduced temperatures. The reference maximum fuel temperature was 1891 K. The annular fuel had a maximum temperature of 1412 K, which is 479 K lower than the reference, and the FCM fuel's maximum temperature was 1092 K, which was 798 K lower than the reference. In terms of maximum

Table 2.9
Specific heat capacity properties.

Material	Specific heat capacity (C_p)[$\frac{J}{kg.K}$]	Mass Weighting	Thermal Conductivity	Reference
UO_2 (n = 1)	Equation 2–3	51.80 %	Equation 2–2	(Popov et al., 2000)
Buffer (n = 2)	1.5	3.10 %	0.5	(Eltawila, 2004)
PyC (n = 3)	1.5	6.37 %	4	(Eltawila, 2004)
SiC (n = 4)	$C_p(T) = 925,65 + 0,3772T - 7,925Z(10^{-5})(T^2) - 3,1946(10^7)(T^{-2})$	7.13 %	Thermal conductivity of polycrystal small grains, as extracted from Figs. 1–3 using Plot Extractor	(Snead et al., 2007)
Matrix (n = 5)	$C_p(T) = 925,65 + 0,3772T - 7,9259(10^{-5})(T^2) - 3,1946(10^7)(T^{-2})$	31.61 %		(Snead et al., 2007)
FCM	$C_{p\,fcm} = \sum_{n=1}^{5} C_{p_n}(\sum_{n=1}^{5} m_n/m_{total})$	100 %	$k_{fcm} = \sum_{n=1}^{5} k_n(\sum_{n=1}^{5} \boldsymbol{m_n}/\boldsymbol{m_{total}})$	

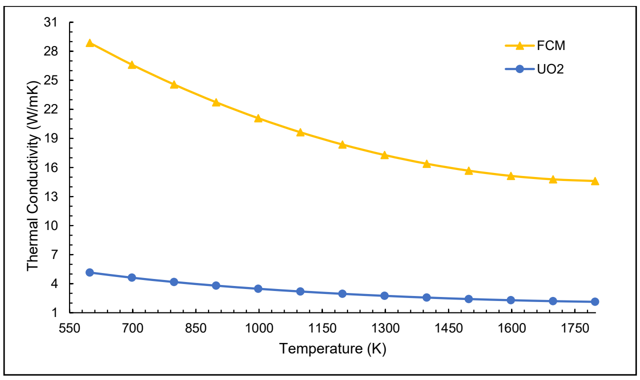

Fig. 2.11. Thermal conductivity of UO_2 and FCM fuel.

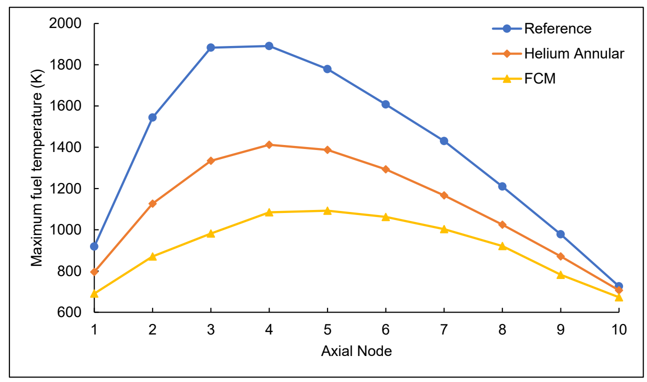

Fig. 2.14. Axial temperature distribution.

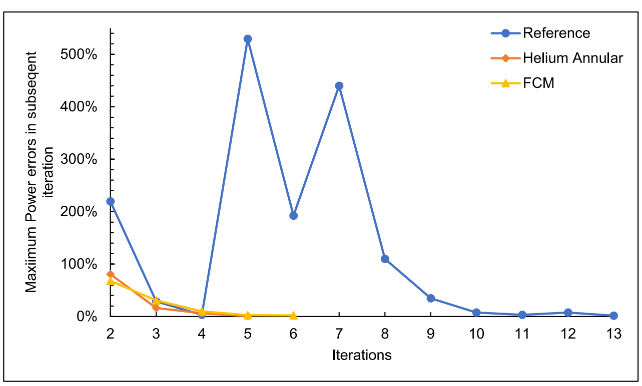

Fig. 2.12. Relative power error in subsequent iterations.

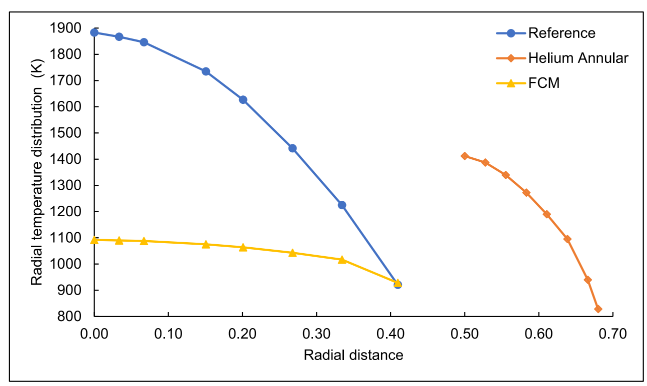

Fig. 2.15. Radial temperature distribution.

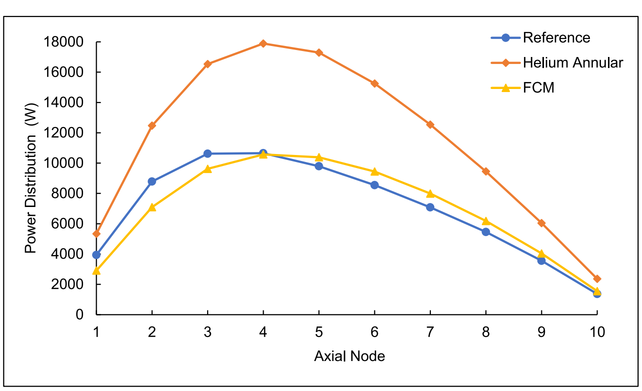

Fig. 2.13. The axial power distribution.

fuel temperature, the FCM fuel was the clear winner. This is to be expected as the thermal conductivity of the FCM is much larger than the reference and helium annular fuel, see Fig. 2.11.

It must be noted that these maximum temperatures are calculated at BOL. It is expected that these maximum temperatures are going to increase as the cycle progresses due to fuel thermal conductivity degradation and change in the fissile material distribution.

Fig. 2.15 shows the radial temperature distribution at the hottest axial node for each fuel, specifically at nodes four and five, as shown in Fig. 2.14. Here, the fourth node corresponds to the reference and helium annulus and the fifth node to the FCM. The peak temperatures align with those in the axial temperature profile shown in Fig. 2.14.

The FCM fuel exhibited a reduced temperature profile owing to its enhanced thermal conductivity. The helium annular fuel also had a reduced maximum temperature compared to the standard reference fuel. This reduction is attributed to the absence of fuel in the central annular void, which typically contributes to higher temperatures. It is important to note that the helium annular fuel exhibited a reduced fuel surface temperature (828.3 K) compared to the reference at 928.5 K (115 % reduction). A reduced fuel surface temperature results in a reduced cladding temperature, which means that there is more grace time before the melting of helium annular fuel compared to the reference and FCM fuels. Both helium annular and FCM ATFs accomplished the goal of reduced central heat accumulation and fuel melting.

3. Conclusion

The study assessed the performance of ATF options for PWRs, focusing on neutronic and thermal–hydraulic aspects such as burnup and maximum fuel temperatures for fresh fuel. Among the ATF options, both annular and FCM fuels exhibit reduced maximum temperatures compared to the reference fuel, with a reduction of 479 K (25.3 %) for annular fuel and 798 K (42.2 %) for the FCM fuel. The lower maximum temperature for ATFs allows more grace time during abnormal operation or accident conditions. This lower fuel temperature also renders better fuel performance and lower fission gas release.

However, when considering neutronic performance in comparison to the reference fuel, the FCM fuel falls short regarding its cycle length by 608 EFPDs but it excels in burnup (79.5 MWd/kgU improvement) due to lower resultant HM loading. To improve the cycle length, it is suggested to use thorium as a fertile element or, even better, use ThUN since nitrides have higher densities. ThN also has a higher thermal conductivity than UO_2 and UN (Du Toit et al., 2024; Gorton et al., 2019). On the other hand, the annular fuel had a burnup improvement of 12.4 MWd/kgU (24.2 %) without the cycle length being affected significantly (5.6 % reduction) compared to the reference fuel.

A fuel performance study is recommended. Even though the FCM performed worse in terms of cycle length, its main purpose is to promote fission product retention which will be superior to that of the annular and reference fuel. The annular fuel will also be advantageous since fission gasses can leak into the central void. It should be noted that the economic aspects were not considered. However, the FCM fuel is expected to be more expensive due to the higher enrichment and more complex TRISO manufacturing. More accurate maximum temperatures for FCM fuel also need to be determined by means of CFD models. Nonetheless, in accidents, it is usually the cladding that fails (melts) first before the fuel due to the lower melting temperatures of cladding as compared to fuel.

These ATFs were only analysed under normal conditions for an average channel at BOL; it is recommended that analyses be carried out for the hot channel and eventual transient accident conditions. Adequate safety coefficients for reactivity feedback and reactivity control need to be investigated for the proposed ATFs. The study can also be extended to perform the depletion calculations with the coupled code system so that the advantages of a lower average fuel temperature on the cycle length can also be confirmed. The lower average fuel temperature may negate the shorter cycle length for FCM fuel.

CRediT authorship contribution statement

Maria Hendrina du Toit: Writing – review & editing, Validation, Supervision, Resources, Project administration, Methodology, Funding acquisition, Conceptualization. **Aubrey Mphofu:** Writing – original draft, Visualization, Software. **Ngoatladi Mashilangako:** Writing – original draft, Software, Investigation.

Declaration of competing interest

The authors declare that they have no known competing financial interests or personal relationships that could have appeared to influence the work reported in this paper.

Data availability

Data will be made available on request.

Acknowledgements

This work is based on the research supported by the Centre for Nuclear Safety and Security through their financial support for the CNSS0319-C4-NWU program.

References

Abdalla, A., Peiman, W., Pioro, I., Gabriel, K., 2012. Sensitivity Analysis of Fuel Centerline Temperature in SCWRs. In: ASME (Ed.), 20th International Conference on Nuclear Engineering. ASME, Anaheim. https://doi.org/10.1115/ICONE20-POWER2012-54530.

Ansarifar, G.R., Esteki, M.H., Zaidabadi, M., 2016. Investigation of the dual-cooled annular fuel effect on the thermal power uprate in a VVER-1000 nuclear reactor. Nucl. Technol. 195, 105–109. https://doi.org/10.13182/NT15-90.

Bowman, S, Suto, T., 1996. SCALE-4 Analysis of Pressurized Water Reactor Critical Configurations: 5.

Bright, L., Eleanor, S., 2019. Understanding UN Nuclear Fuel : A Study of the Fundamental Physical Behaviour and Degradation of Uranium Nitrides.

Brown, N.R., Hernandez, R., Nelson, A.T., 2022. High volume packing fraction TRISO-based fuel in light water reactors. Prog. Nucl. Energy 146, 104151. https://doi.org/10.1016/j.pnucene.2022.104151.

Ćalić, D., Žerovnik, G., Trkov, A., Snoj, L., 2016. Validation of the Serpent 2 code on TRIGA Mark II benchmark experiments. Appl. Radiat. Isot. 107, 165–170. https://doi.org/10.1016/J.APRADISO.2015.10.022.

Carpenter, D.M., 2006. Assessment of Innovative Fuel Designs for High Performance Light Water Reactors.

Deng, Q., Li, S., Wang, D., Liu, Z., Xie, F., Zhao, J., Liang, J., Jiang, Y., 2022. Neutronic design and evaluation of the solid microencapsulated fuel in LWR. Eng. Technol. Nucl. https://doi.org/10.1016/j.net.2022.03.020.

Deng, Y., Liu, M., Qiu, B., Yin, Y., Gong, X., Huang, X., Pang, B., Li, Y., 2021. Design and evaluation of an innovative LWR fuel combined dual-cooled annular geometry and SiC cladding materials. Nucl. Eng. Technol. 53, 178–187. https://doi.org/10.1016/j.net.2020.06.025.

Dobisesky, J., Richard, J., Pilat, E.E., Kazimi, M.S., Carpenter, D.M., 2014. Fuel management of pwr cores with silicon carbide cladding. Nucl. Technol. 186, 353–377. https://doi.org/10.13182/NT12-131.

Du Toit, M.H., Niekerk, V., Frederik Amirkhosravi, S., 2024. Review of thorium-containing fuels in LWRs. Prog. Nucl Energy 170, 105136. https://doi.org/10.1016/j.pnucene.2024.105136.

Ellis, T.S., 2006. Advanced Design Concepts for PWR and BWR High-Performance Annular Fuel Assemblies. Massachusetts Institute of Technology.

El-Sahlamy, N., Hassan, M., Khedr, A., 2020. Comparison between standard solid fuel and a new annular fuel performance in the core of a PWR. Kerntechnik. https://doi.org/10.3139/124.190020.

Eltawila, F., 2004. TRISO-Coated Particle Fuel Phenomenon identification and ranking tables (PIRTs) for Fission Product Transport Due to Manufacturing, Operations, and Accidents, NUREG/CR-6844. Nuclear Regulatory Commission, Washington.

Feng, D., Hejzlar, P., Kazimi, M.S., Feng, D., Hejzlar, P., Kazimi, M.S., 2017. Thermal-hydraulic design of high-power-density annular fuel in PWRs. Nucl. Technol. 160, 16–44. https://doi.org/10.13182/NT07-A3882.

Flownex SE, 2022. Flownex SE [WWW Document]. URL https://flownex.com/industries/nuclear-smr/.

Gorton, J.P., Collins, B.S., Nelson, A.T., Brown, N.R., 2019. Reactor performance and safety characteristics of ThN-UN fuel concepts in a PWR. Nucl. Eng. Des. 355, 110317 https://doi.org/10.1016/j.nucengdes.2019.110317.

Hakim, A.R., Harto, A.W., Agung, A., 2019. Neutronic analysis of fuel assembly design in Small-PWR using uranium mononitride fully ceramic micro-encapsulated fuel using SCALE and Serpent codes. Nucl. Eng. Technol. 51, 1–12. https://doi.org/10.1016/j.net.2018.08.007.

Hejzlar, P., Kazimi, M.S., 2008. Final Technical Report for the MIT Annular Fuel Research Project.

Hejzlar, P., Kazimi, M.S., 2007. Annular fuel for high-power-density pressurized water reactors: Motivation and overview. Nucl. Technol. 160, 2–15. https://doi.org/10.13182/NT160-2-15.

IAEA, 2014. Accident Tolerant Fuel Concepts for Light Water Reactors | IAEA [WWW Document].

Kaltiaisenaho, T., 2020. Photon transport physics in Serpent 2 Monte Carlo code. Comput. Phys. Commun. 252, 107143 https://doi.org/10.1016/j.cpc.2020.107143.

Kavazauri, R., Pokrovskiy, S.A., Baranov, V.G., Tenishev, A.V., 2016. Thermal properties of nonstoichiometry uranium dioxide. IOP Conf. Ser. Mater. Sci. Eng. 130 https://doi.org/10.1088/1757-899X/130/1/012025.

Keun, C., Chang, J., Venneri, F., Hawari, A., 2014. Preliminary core analysis of a micro modular reactor. Trans. Korean Nucl. Soc. Spring Meet 4.

Kianpour, R., Ansarifar, G.R., Fathi, M., 2020. Optimal design of a VVER-1000 nuclear reactor core with dual cooled annular fuel based on the reactivity temperature coefficients using Thermal hydraulic and neutronic analysis by implementing the genetic algorithms. Ann. Nucl. Energy 148, 107682. https://doi.org/10.1016/j.anucene.2020.107682.

Koo, Y.H., Yang, J.H., Park, J.Y., Kim, K.S., Kim, H.G., Kim, D.J., Jung, Y.I., Song, K.W., 2014. Kaeri's development of LWR accident-tolerant fuel. Nucl. Technol. 186, 295–304. https://doi.org/10.13182/NT13-89.

Leppänen, J., 2011. Serpent – a Continuous-energy Monte Carlo reactor physics burnup calculation code. Tech. Res. Cent Finl. 157.

Leppänen, J., Pusa, M., Viitanen, T., Valtavirta, V., Kaltiaisenaho, T., Carlo, M., 2014. The Serpent Monte Carlo code: Status, development and applications in 2013, Ann. Nucl. Energy. https://doi.org/10.1016/j.anucene.2014.08.024.

Liu, R., Prudil, A., Zhou, W., Chan, P.K., 2016. Multiphysics coupled modeling of light water reactor fuel performance. Prog. Nucl. Energy 91, 38–48. https://doi.org/10.1016/j.pnucene.2016.03.030.

Liu, H., 2018. Hihg Temperature Degradation of Silicon Carbide (SIC) by Metallic Fission Products (Palladium, Silver) and Oxidation. A thesis Submitt. to Univ. Manchester degree Dr. Philos. Mater. Sci. The University of Manchester.

Mizokami, S., Rempe, J.L., 2020. The Events at Fukushima Daiichi, Reference Module in Earth Systems and Environmental Sciences. Elsevier Inc. https://doi.org/10.1016/b978-0-12-409548-9.12148-7.

Morris, R.N., Pappano, P.J., 2007. Estimation of maximum coated particle fuel compact packing fraction. J. Nucl. Mater. 361, 18–29. https://doi.org/10.1016/j.jnucmat.2006.10.017.

Mulasi, C., 2022. Criticality study of a spent fuel pool using SCALE 6.2.3 and MCNP6.2.

NRC, 2016. North Anna Power Station Updated Final Safety Analysis Report Chapter 1.

Pane, D.N., EL Fikri, M., Ritonga, H.M., 2018. Modeling approach for annular-fuel elements using the assert-pv subchannel code. J. Chem. Inf. Model. 53, 1689–1699.

Popov, S., Carbajo, J., Ivanov, V., Yoder, G., 2000. Thermophysical Properties of MOX and UO2 Fuels Including the Effects of Irradiation. ORNL, Oak Ridge.

Powers, J., Lee, W.J., Snead, L., Venneri, F.G.V., Jo, C.K., Hwang, D.H., Chun, J.H., Kim, Y.M., Terrani, K.A., 2013. Fully Ceramic Microencapsulated (FCM) Replacement Fuel for LWRs. Tennessee.

Safavi, A., Hossein, M., Mohammad, S., 2020. Application of a new neutronics / thermal-hydraulics coupled code for steady state analysis of light water reactors. Nucl. Eng. Technol. 52, 1603–1610. https://doi.org/10.1016/j.net.2020.01.024.

Schappel, D.P., 2017. Improvements to the Predictive Capability of FCM Fuel Performance Modeling. Tennessee Res. Creat. Exch. Dr. Tennessee, Knoxv.

Scolaro, A., Uffelen, P.V., Schubert, A., Fiorina, C., Brunetto, E., Clifford, I., Pautz, A., 2022. Progress in nuclear energy towards coupling conventional with high-fidelity fuel behavior analysis tools. Prog. Nucl. Energy 152, 104357. https://doi.org/10.1016/j.pnucene.2022.104357.

Silva, R.H.M., Ramos, M.C., Velasquez, C.E., Clarysson, A.M., Pereira, C., Costa, A.L., 2017. Neutronic evaluation of annular fuel rods to assemblies 13X13, 14X14 and 15X15. International Nuclear Atlatic Conference. Associação Brasileira De Energia Nuclear, Belo Horizonte.

Singh, G., Sweet, R., Brown, N.R., Wirth, B.D., Katoh, Y., Terrani, K., 2018. Parametric evaluation of SiC/SiC composite cladding with UO2 fuel for LWR applications: fuel rod interactions and impact of nonuniform power profile in fuel rod. J. Nucl. Mater. 499, 155–167. https://doi.org/10.1016/j.jnucmat.2017.10.059.

Slabber, J., 2014. Is silicon carbide a solution to safer light-water reactor fuel? Innovate 48–51.

Snead, L.L., Nozawa, T., Katoh, Y., Byun, T.S., Kondo, S., Petti, D.A., 2007. Handbook of SiC properties for fuel performance modeling. J. Nucl. Mater. 371, 329–377. https://doi.org/10.1016/j.jnucmat.2007.05.016.

Terrani, K.A., Jolly, B.C., Trammell, M.P., Vasadevamurthy, G., Schappel, D., Ade, B., Helmreich, G.W., Wang, H., Rossy, A.M., Betzler, B.R., Nelson, A.T., 2021. Architecture and properties of TCR fuel form. J. Nucl. Mater. 547, 152781 https://doi.org/10.1016/j.jnucmat.2021.152781.

Valtavirta, V., 2017. Coupled calculations with Serpent 2.1.29. 7th Int. Serpent User Gr. Meet.

Van Der Merwe, J.J., Bollen, R., Van Ravenswaay, J.P., 2006. Validation and verfication of Flownex nuclear. In: 3rd International Topical Meeting on High Temperature Reactor Technology. IAEA, Johannesburg, pp. 1–6.

van Ravenswaay, J.P., Greyvenstein, G.P., van Niekerk, W.M.K., Labuschagne, J.T., 2006. Verification and validation of the HTGR systems CFD code Flownex. Nucl. Eng. Des. 236, 491–501. https://doi.org/10.1016/j.nucengdes.2005.11.025.

Yarmohammadi, M., Rahgoshay, M., Shirani, A.S., 2017. Effect of central hole on fuel temperature distribution. Nucl. Eng. Technol. 49, 1629–1635. https://doi.org/10.1016/j.net.2017.07.022.

Ye, L., Wang, M., Wang, X., Deng, J., Xiang, Y., Tian, W., Qiu, S., Su, G.H., 2020. Thermal hydraulic and neutronics coupling analysis for plate type fuel in nuclear reactor core. Sci. Technol. Nucl. Install. 2020 https://doi.org/10.1155/2020/2562747.

Yueh, K., Terrani, K.A., 2014. Silicon carbide composite for light water reactor fuel assembly applications. J. Nucl. Mater. 448, 380–388. https://doi.org/10.1016/j.jnucmat.2013.12.004.

Zhuchkovaa, A., Nava-dominguez, A., 2014. Thermal-hydrualic model of annular fuel of pressurized heavy water reactor. Ontario.